Interaction of NLS Solitons with defects: Numerical Experiments and Finite-dimensional modeling

Roy H. Goodman* Philip J. Holmes† Michael I. Weinstein‡

February 28, 2002

Abstract

We consider the interaction of a nonlinear Schrödinger soliton with a localized (point) defect in the medium through which it travels. Using numerical simulations, we find parameter regimes under which the soliton may be reflected, transmitted, or captured by the defect. We propose a mechanism of resonant energy transfer to a nonlinear standing wave mode supported by the defect. Following Forinash et. al. [2], we derive a finite-dimensional model for the interaction of the soliton with the defect via a collective coordinates method. The system thus derived is a three degree-of-freedom Hamiltonian with an additional conserved quantity. We study this system using the tools of dynamical systems theory, and find that it exhibits a variety of interesting behaviors, largely determined by the structures of stable and unstable manifolds of special classes of periodic orbits. We use this geometrical understanding to interpret the simulations.

Dedicated to Klaus Kirchgässner on the occasion of his seventieth birthday.

1 Introduction

In a previous study of the propagation of nonlinear pulses of light through Bragg grating optical fibers with localized defects, we suggested a way to design specialized defect which could be used to trap and localize light [4]. The technique involves resonant transfer of energy from traveling waves (gap solitons) to standing wave modes localized on the defect. The cubic nonlinear Schrödinger (NLS)

*Mathematical Sciences Department, New Jersey Institute of Technology, Newark, NJ 07102

†Program in Applied and Computational Mathematics and Department of Mechanical and Aerospace Engineering, Princeton University, Princeton, NJ 08544

‡Mathematical Sciences Research, Bell Laboratories–Lucent Technologies, Murray Hill, NJ 07974

equation with localized potentials provides a simpler and more fully-analyzable model that exhibits similar phenomena, and we study it in this paper. In particular, in numerical simulations of NLS solitons incident on a single delta-well (point) defect, we find a variety of behaviors, including nearly elastic transmission and reflection, capture, and strongly inelastic transmission, depending on the parameters describing the soliton.

Several studies have examined the propagation of nonlinear waves through variable or random media. A common approach to this problem is to assume that the medium is uniform, interrupted by a sequence of Dirac delta-like potentials, and then to sum up the soliton's interactions with many of these localized defects. Many of these studies focus on the loss of soliton energy to radiation in such systems in the weak interaction regime (eg. [8, 1]), whereas we focus here on the possibility of soliton capture at a defect location as a result of strong interactions.

We proceed in two steps. First we conduct a series of numerical experiments on the partial differential equation (PDE), in which a variety of of phenomena are observed, which we may partly explain by a resonant transfer of energy to standing wave modes localized at the defect. This work is not reported here, but will be included in a subsequent paper. Second, we derive a finite dimensional system of ordinary differential equations (ODEs) that models the interaction of solitons with nonlinear standing wave modes or 'defect modes' supported by the potential. This part of the analysis, on which we focus here, is similar in spirit to our earlier study of a finite dimensional reduction of the simpler case of kinks interacting with a trapped mode in the sine-Gordon equation with a point defect [3]. After reviewing the basic PDE model in Section 2, we outline the (formal) finite-dimensional reduction procedure in Section 3 and describe some invariant subspaces and special sets of orbits of the resulting ODE system. We then describe in Section 4 a representative set of three numerical experiments that reveal the range of soliton transmission, reflection and transient capture behaviors that the ODEs exhibit. Section 5 returns to analysis of the ODEs, in particular focusing on the stable and unstable manifolds of certain periodic orbits, that are shown to partially 'organize' the global dynamics, providing separatrices between transmitted and reflected soliton orbits. We summarize in Section 6.

In offering this work-in-progress as a tribute to Klaus Kirchgässner, we trust that the geometrical flavor of our analysis will be seen as a small homage to his elegant use of dynamical systems ideas in the study of nonlinear waves, and that our results, both partial and ordinary, may likewise open new paths in the study of differential equations.

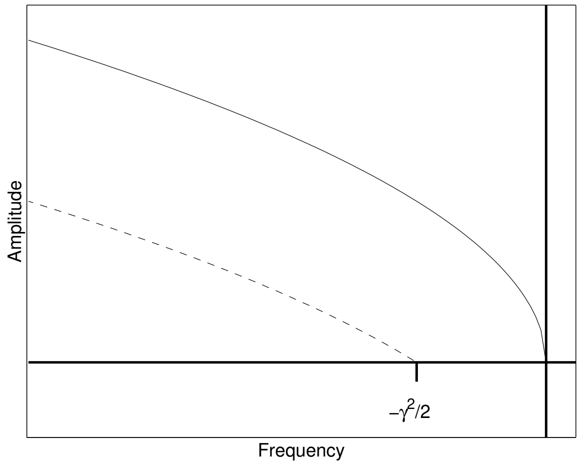

Figure 2.1: The frequency and amplitude of a soliton in the absence of a defect (solid), and of the defect mode (dashed).

2 The nonlinear Schrödinger (NLS) equation with a point defect

We consider a nonlinear Schrödinger (NLS) equation with a localized impurity at the origin:

$$iu_t + \frac{1}{2}u_{xx} + |u|^2 u + \gamma\,\delta(x)u = 0. \tag{2.1}$$

In the absence of a defect ($\gamma = 0$), this system supports solitons of the form

$$u_{\rm Sol}(x,t) = \eta\,\mathrm{sech}(\eta(x - Vt))e^{i(Vx-\omega t)} \tag{2.2}$$

where $\omega = -\frac{1}{2}(\eta^2 - V^2)$ is the temporal frequency. Far from the defect, these solitons propagate at constant speed, while maintaining their shapes.

Equation (2.1) also supports *exact* nonlinear bound state or defect mode solutions of the form

$$u_{\rm Def}(x,t) = ae^{ia^2t/2}\,\mathrm{sech}\,(a|x| + \tanh^{-1}\frac{\gamma}{a}), \tag{2.3}$$

for all $a \geq \gamma$. These solutions simply correspond to a stationary ($V = 0$) soliton on each side of the defect pasted together at $x = 0$ to satisfy the appropriate jump condition in the first derivative. For these bound states, the frequency of oscillation depends nonlinearly on its amplitude.

Solitons with $V = 0$ have $\|u_{\rm Sol}\|^2 = 2\eta$ and frequency $-\eta^2/2$, whereas nonlinear defect modes have $\|u_{\rm Def}\|^2 = 2(a-\gamma)$ and frequency $-a^2/2$. In Figure 2.1 we plot the norm squared of these two types of mode as functions of frequency.

Note that no defect modes exist in the frequency range $\omega \in (-\gamma^2/2, 0]$. This observation is crucial in predicting which solitons will be trapped and which reflected by the potential. We find, roughly, that sufficiently slow solitons with $\eta > \gamma$ are trapped upon encountering the defect, while slow solitons with $\eta < \gamma$ are reflected by the defect. This suggests that trapping occurs via resonant energy transfer from the soliton to the defect mode. If the incoming soliton has frequency less than $-\gamma^2/2$, it can and may excite a nonlinear defect mode and transfer its energy to that mode. Otherwise, the defect mode cannot ultimately absorb the energy from the incoming soliton, and the wave is transmitted or reflected nearly elastically. Similar behavior occurs in a related problem in optics: the nonlinear coupled mode equations describing the interaction of gsp solitons with nonlinear defect modes [4].

Direct numerical simulations of the PDE (2.1) illustrating these phenomena will be reported in an extended version of this article.

3 A model of soliton-defect interaction

3.1 Two mode ansatz, Lagrangian and Hamiltonian formulations

Forinash, Peyrard, and Malomed [2] study the interaction of a soliton with a linear defect mode by using a collective coordinate ansatz to derive a set of approximate equations to describe the evolution of a finite set of variables that characterize the two modes. We slightly simplify and modify their ansatz to allow for a *nonlinear* bound state u_{Def}, setting $u = u_{\mathrm{S}} + u_{\mathrm{D}}$, where u_{S} is a generalized soliton of the form

$$u_{\mathrm{S}} = \eta \operatorname{sech}(\eta x - Z)\, e^{i(Vx-\phi)}, \tag{3.1}$$

and u_{D} is a generalized bound state of the form

$$u_{\mathrm{D}} = a \operatorname{sech}\left(a|x| + \tanh^{-1}\frac{\gamma}{a}\right) e^{-i(\phi+\psi)}. \tag{3.2}$$

In (3.1, 3.2), the variables η, Z, V, ϕ, a, and ψ are all allowed to depend on t. The Lagrangian functional of the NLS equation is evaluated at u (by integrating over the spatial domain), and the resulting function is then interpreted as a finite-dimensional Lagrangian whose Euler-Lagrange equations determine the evolution of these variables. Instead of extremizing the (true) Lagrangian with respect to admissible variations of the field variable $u(x,t)$, we effectively consider only variations in the subspace spanned by the time-dependent variables of the ansatz. A similar strategy was employed in [7, 9] to investigate wave propagation in NLS with periodically varying dispersion.

The Lagrangian for NLS is

$$\mathcal{L} = \int_{-\infty}^{\infty} \frac{i}{2}(u^* u_t - u u_t^*) - \frac{1}{2}|u_x|^2 + \frac{1}{2}|u|^4 + \gamma\delta(x)|u|^2 dx.$$

We evaluate this for our ansatz u. Unlike [2] and most other analyses of this type of which we are aware, we do not assume that a is small, and we include high-order terms involving a. We do assume that all interaction between the modes u_{S} and u_{D} takes place through terms involving the delta function. This is, in part, justified because the other interaction terms involve oscillatory integrals which will average out to be much smaller than the terms retained. The resulting effective Lagrangian is given by

$$\mathcal{L}_{\mathrm{eff}} = 2\eta\dot{\phi} - 2Z\dot{V} + 2(a-\gamma)(\dot{\phi}+\dot{\psi}) + \frac{1}{3}\eta^3 - \eta V^2 + \frac{1}{3}a^3 + \gamma\eta^2 \operatorname{sech}^2 Z + 2\gamma\eta\sqrt{a^2-\gamma^2}\operatorname{sech} Z \cos\psi. \tag{3.3}$$

This Lagrangian has an associated Hamiltonian, conserved by the Euler Lagrange (and Hamilton's) equations:

$$H = -\frac{1}{3}\eta^3 + \eta V^2 - \frac{1}{3}a^3 - \gamma\eta^2 \operatorname{sech}^2 Z - 2\gamma\eta\sqrt{a^2-\gamma^2}\operatorname{sech} Z \cos\psi, \tag{3.4}$$

in which the variables V, ϕ, and ψ correspond to generalized positions and the generalized momenta are given by

$$p_V = \frac{\partial \mathcal{L}_{\mathrm{eff}}}{\partial \dot{V}} = -2Z, \tag{3.5}$$

$$L \stackrel{\mathrm{def}}{=} p_\phi = \frac{\partial \mathcal{L}_{\mathrm{eff}}}{\partial \dot{\phi}} = 2\eta + 2(a-\gamma), \tag{3.6}$$

$$I \stackrel{\mathrm{def}}{=} p_\psi = \frac{\partial \mathcal{L}_{\mathrm{eff}}}{\partial \dot{\psi}} = 2(a-\gamma). \tag{3.7}$$

In canonical coordinates, the Hamiltonian becomes

$$H = -\frac{1}{24}(L-I)^3 + \frac{1}{2}(L-I)V^2 - \frac{1}{3}(\frac{I}{2}+\gamma)^3 - \frac{\gamma}{4}(L-I)^2 \operatorname{sech}^2 \frac{p_V}{2} - \frac{\gamma}{2}(L-I)\sqrt{I(I+4\gamma)}\operatorname{sech}\frac{p_V}{2}\cos\psi, \tag{3.8}$$

which is independent of ϕ. The conjugate momentum $L = 2\eta + 2(a-\gamma)$ is therefore a constant of the motion and the evolution of ϕ can be determined by a quadrature. From the discussion following Equations (2.2-2.3), we have $L = \|u_{\mathrm{S}}\|^2 + \|u_{\mathrm{D}}\|^2$, so this corresponds to the physical fact that, while energy transfer between the two modes can occur, the total L^2 energy is still conserved in this model.

The phase space of this three degree-of-freedom system can be therefore be expressed as the cross product of the 4-dimensional (V,ψ,P_V,I)-phase space and the 2-dimensional (ϕ,L)-phase space, with trivial dynamics on the latter. In the analysis that follows, we may therefore regard L as a parameter determined by the initial conditions, and study the reduced Hamiltonian system defined by $H(V,\psi,p_V,I;L)$ on the (V,ψ,p_V,I)-phase space. However, it is more convenient to work in a slightly modified version of the Lagrangian coordinates. Since $\eta + a - \gamma = L/2$ remains constant, we may set

$$\eta = c - a, \quad \text{with } c = L/2 + \gamma,$$

as a new constant parameter, and work with the variables (Z, V, ψ, a). In terms of these, the reduced evolution equations are:

$$\dot{Z} = (c-a)V, \tag{3.9a}$$

$$\dot{V} = -\gamma(c-a)^2 \operatorname{sech}^2 Z \tanh Z - \gamma(c-a)\sqrt{a^2-\gamma^2}\operatorname{sech} Z \tanh Z \cos\psi, \tag{3.9b}$$

$$\dot{\psi} = \frac{(c-a)^2 - a^2 - V^2}{2} + \gamma(c-a)\operatorname{sech}^2 Z + \gamma\frac{2a^2-\gamma^2-ac}{\sqrt{a^2-\gamma^2}}\operatorname{sech} Z\cos\psi, \tag{3.9c}$$

$$\dot{a} = -\gamma(c-a)\sqrt{a^2-\gamma^2}\operatorname{sech} Z \sin\psi. \tag{3.9d}$$

and ϕ evolves according to:

$$\dot{\phi} = -\frac{(c-a)^2 - V^2}{2} - \gamma(c-a)\operatorname{sech}^2 Z - \gamma\sqrt{a^2-\gamma^2}\operatorname{sech} Z\cos\psi. \tag{3.10}$$

3.2 The rescaled, reduced system: initial analysis

A further simplification results from the following rescaling: $a \mapsto \gamma a$, $c \mapsto \gamma c$, $t \mapsto t/\gamma^2$: implying that, without loss of generality, the parameter γ may be set to equal to one. Then c is the only parameter remaining in the evolution equations, and these equations are in fact canonically Hamiltonian for the 'scaled' Hamiltonian $H/2$, with H of (3.8) written in the Lagrangian coordinates:

$$H(Z,V,\psi,a) = -\frac{c^3}{3} + (c-a)\left(ca + V^2 - (c-a)\operatorname{sech}^2 Z\right) - 2(c-a)\sqrt{a^2-1}\operatorname{sech} Z\cos\psi. \tag{3.11}$$

The final reduced equations, to be studied below, are now:

$$\dot{Z} = (c-a)V, \tag{3.12a}$$

$$\dot{V} = -(c-a)^2\operatorname{sech}^2 Z\tanh Z - (c-a)\sqrt{a^2-1}\operatorname{sech} Z\tanh Z\cos\psi, \tag{3.12b}$$

$$\dot{\psi} = \frac{c^2 - 2ca - V^2}{2} + (c-a)\operatorname{sech}^2 Z + \frac{(2a^2 - ca - 1)}{\sqrt{a^2-1}}\operatorname{sech} Z\cos\psi, \tag{3.12c}$$

$$\dot{a} = -(c-a)\sqrt{a^2-1}\operatorname{sech} Z\sin\psi. \tag{3.12d}$$

We note that the sets $a = c$ and $a = 1$ are invariant (although the vector field is singular on the latter), and bound the physically admissible region. When

$a = 1$ all the energy resides in the soliton, when $a = c$ it all resides in the defect mode. Letting $\mathcal{I} = [1, c]$ denote the closed interval, the phase space of Equation (3.12) is $(Z, V, \psi, a) \in \mathbb{R}^2 \times S^1 \times \mathcal{I}$. We also note the following symmetry group under which (3.12) is equivariant:

$$(Z, V, \psi, a, t) \to (-Z, V, 2\pi - \psi, a, -t), \tag{3.13a}$$

$$(Z, V, \psi, a, t) \to (Z, -V, 2\pi - \psi, a, -t). \tag{3.13b}$$

This will be useful later.

There is a family of solutions at $Z = \pm\infty$ with V, a, and $\dot{\psi}$ constant, which correspond to the uncoupled propagation and oscillation of the two modes when the soliton is infinitely far from the defect. The subset of these solutions with $V = 0$ form a degenerate family of periodic orbits, parameterized by $a = a_\infty$ and filling the annulus (or finite cylinder) $\mathcal{P}_\infty = \{(\psi, a) | V = 0,\ |Z| = \infty\}$. As in [3] we may employ a transformation of the form $q = \operatorname{sech} Z,\ p = V$ to bring these orbits to the origin in (p, q)-space, and then apply McGehee's stable manifold theorem [10] to prove the existence of invariant manifolds for the fixed point $(p, q) = (0, 0)$ in an appropriate (local) Poincaré map. This shows that each periodic orbit in $\mathcal{P}_\infty$ has two-dimensional stable and unstable manifolds, so that $W^s(\mathcal{P}_\infty)$ – the stable manifold of $\mathcal{P}_\infty$ itself – is three dimensional and hence separates the four-dimensional phase space. Indeed, $W^s(\mathcal{P}_\infty)$ locally separates orbits that escape to infinity (transmitted solitons) from those that are reflected to interact with the defect mode again.

Studying the analogous sine-Gordon problem in [3], we used isoenergetic reduction and Melnikov's method [11, 5] to prove that the stable and unstable manifolds of each periodic orbit, restricted to their common energy manifold, intersect transversely and hence that Smale horseshoes exist. We then appealed to phase space transport theory [12, 13] to unravel the structure of sets of initial data that are transiently captured before eventually being transmitted or reflected. While we can proceed in the same manner here, the reduction procedure requires that the frequency $\dot{\psi}$ not change sign (one replaces time by ψ), and this holds only for large c, depending on a; cf. Equation (3.12c). In particular, it does *not* hold for many physically relevant parameter values, including those corresponding to initial data with (almost) all the energy in the soliton ($a \approx 1$).

However, there are some further invariant manifolds that play an important rôle in the fate of solutions. They belong to orbits on a second annulus $\mathcal{P}_0 = \{(\psi, a) | V = 0,\ Z = 0\}$ that is also invariant under the flow, and on which the ODEs are integrable. Solutions on $\mathcal{P}_0$ correspond to a soliton stalled over the defect and periodically exchanging energy with the defect mode. The orbit structure on $\mathcal{P}_0$ depends upon c and may be derived from the level sets of the Hamiltonian function H restricted to $\mathcal{P}_0$:

$$H_0(\psi, a) = -\frac{c^3}{3} + (c - a)\left(ca - (c - a) - 2\sqrt{a^2 - 1}\cos\psi\right). \tag{3.14}$$

As noted above, the boundaries $a = c$ and $a = 1$ of $\mathcal{P}_0$ are invariant, and the flow is singular on the latter, which contains two degenerate saddle points

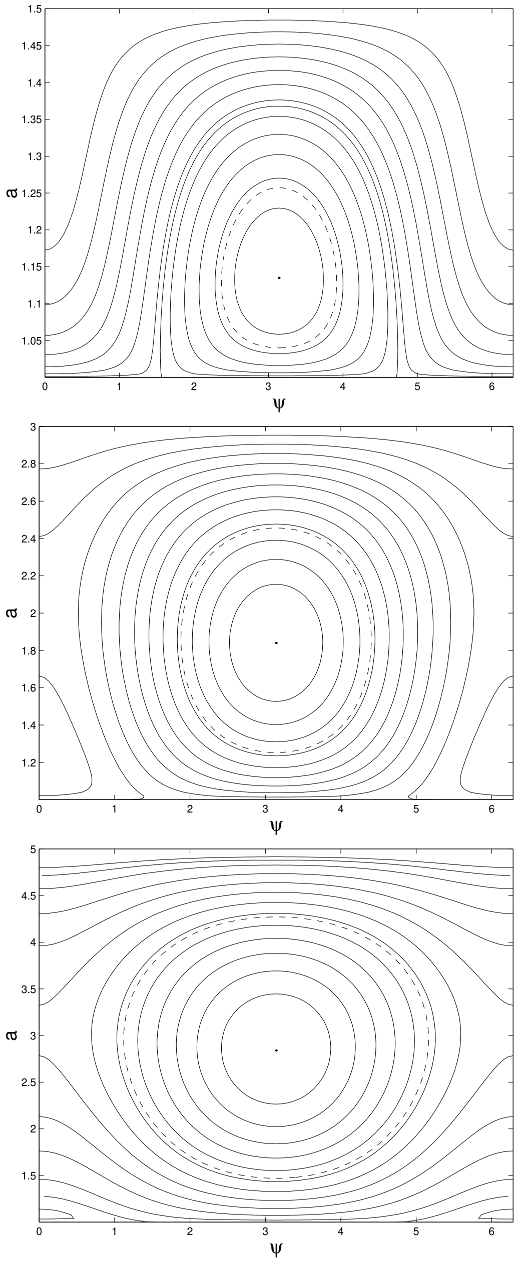

Figure 3.1: Level sets of H_0 in the invariant plane $\mathcal{P}_0$ for (a): $c = 1.5$; (b) $c = 3$ and (c) $c = 5$. The dashed curve indicates the boundary of the orbits accessible from infinity, as described in the text.

at $\psi = \pi/2,\ 3\pi/2$. There is a unique fixed point (π, a^*) on $\psi = \pi$ surrounded by periodic orbits which limit on heteroclinic orbit(s). As shown in the Appendix, for all c (> 1), (π, a^*) is a saddle-center, with positive and negative real eigenvalues whose eigenvectors point out of $\mathcal{P}_0$. For $c < 2.214\ldots$ this is the only equilibrium; for $c > 2.214\ldots$ two further fixed points, a center-center and a saddle-center, appear on $\psi = 0$; restricted to $\mathcal{P}_0$ these are a center and a saddle, whose separatrices interact with the stable and unstable manifolds of the degenerate saddles on $a = 1$ in a heteroclinic bifurcation [5] at $c \approx 3.21$ as c continues to increase. H_0 takes its minimum value $-c^3/3$ on $c = a$, its maximum at (π, a^*), and the value $-c^3/3 + c - 1$ on $a = 1$ and the invariant manifolds emanating from it. Figure 3.1 shows three representative cases. On this figure we also show the level set with Hamiltonian value equal to that of a 'pure' soliton stalled at infinity: $H(|Z| = \infty, V = 0, a = 1, \psi) = -c^3/3 + c(c-1)$. Since any incoming soliton with nonzero speed has $H > -c^3/3 + c(c-1)$ (see (3.11)), this curve bounds the set of *accessible* orbits on $\mathcal{P}_0$: a disk centered on (π, a^*).

To determine the stable and unstable manifolds of $\mathcal{P}_0$ we must first determine the stability types of orbits within it, to perturbations out of $\mathcal{P}_0$. By continuity, the periodic orbits immediately surrounding (π, a^*) are also of saddle type with respect to such perturbations, but the stability types of other periodic orbits must be determined via Floquet theory [6]. Before doing this (in Section 5.1), we describe some numerical experiments on the ODE system (3.12) that reveal interesting interactions between the soliton and the defect mode, and suggest more specific analyses.

4 ODE Simulations of the initial value problem

In the following numerical experiments we initialize a soliton at $Z(0) = -Z_0$ with $|Z_0| \gg 1$, far from the defect, with amplitude η and velocity $V(0) = v_{\rm in} > 0$, propagating rightward toward the defect. We use $|Z_0| = 20$ for the computations below. We assume there is no energy initially in the defect mode, so $a(0) = 1$ and $\eta = c - a(0)$ thereby fixes the constant c. (In fact, because of the singularity of Equation (3.12c) at $a = 1$, we set $a(0) = 1 + \varepsilon$, where $\varepsilon \ll 1$; we used the value $\varepsilon = 10^{-5}$ in these computations. One can also work with a version of Equations (3.12) with time reparameterized via $t \mapsto (\sqrt{a^2 - 1})\ t$, effectively multiplying the right hand side by $\sqrt{a^2 - 1}$ and removing the singularities.) Finally, we set $\psi(0) = 0$. Note that, for large $|Z|$, the ψ dependence becomes exponentially weak, so we do not expect strong ψ-dependent effects.

We choose a representative set of η (c) values and for each fixed η allow $v_{\rm in}$ to vary over a range of values, for each of which we numerically integrate (3.12) until the soliton reaches the defect, (eventually) exits the defect region, and reaches $|Z| = Z_0$ at, say $t = T$. (By a variant of the Poincaré recurrence theorem, as in [3], we can show that the soliton must eventually escape any bounded set containing the defect.) We then plot the soliton's outgoing velocity $V(T) = v_{\rm out}$ and the amplitude $(a(T) - 1)$ of the defect mode as functions of

v_{in}. For Z_0 sufficiently large and ε sufficiently small, the initial value of the phase difference ψ was indeed found to be unimportant in determining the values of $V(T)$ and $(a(T)-1)$. Our η choices were guided by initial explorations and the differing phase portraits on $\mathcal{P}_0$ illustrated in Figure 3.1. In interpreting these results, it is important to realize that the dynamics takes place in four-dimensional phase space, and that the figures merely show projections of trajectories on lower dimensional subspaces.

4.1 Experiment 1: small η.

We observe several distinct types of behavior. In Figure 4.1, $\eta = \frac{1}{2} < \gamma$; in this case the soliton is reflected if v_{in} is below a critical velocity $v_c \approx 0.51$ and transmitted if $v_{\text{in}} > v_c$. We also see that the defect mode has a final amplitude of order 10^{-3}, absorbing little of the soliton's mass. We note that $-\gamma^2/2 = -1/2 < -\eta^2/2$ corresponds to the region in Figure 2.1 in which the soliton has no resonant defect mode 'partner' with the same temporal frequency, and hence that appreciable interactions are unlikely [4].

Figure 4.2 shows evidence that the solution passes near $Z = V = 0$, presumably approaching and leaving the neighborhood of a hyperbolic fixed point or periodic orbit on $\mathcal{P}_0$. Indeed, in the figure we also show projections onto (Z, V)-space of the numerically determined stable and unstable manifolds of the fixed point $W^{s,u}(\pi, a^*)$, along with two trajectories: one with asymptotic velocity larger than the limiting value on the unstable manifold, which is transmitted, and one with asymptotic velocity smaller than the limiting velocity, which is reflected.

4.2 Experiment 2: medium η.

In Figure 4.3, computed for $\eta = 2$, we see a quite different picture. Here and in the third case, below, $-\eta^2/2 < -\gamma^2/2 = -1/2$ and resonant interactions can and do take place. In this case there is no transition between transmission and reflection: the soliton travels monotonically rightward and is *always* transmitted without ever oscillating about the defect. More strikingly, the output velocity appears to approach a finite limit $v_{\text{out}} \approx 1.17$ as $v_{\text{in}} \to 0$, while the amount of mass captured approaches $a - 1 \approx 1.26$ (all the soliton's mass would be captured if $a - 1 = 2$). As the initial velocity increases, so does the output velocity, while the mass transferred from the soliton to the defect mode decreases. This is not surprising, since the duration of the interaction decreases with increasing soliton speed.

4.3 Experiment 3: large η.

Yet different behavior emerges when we increase η to 4, as illustrated in Figure 4.4. In this case we find a sharp change in behavior at a critical velocity $v_c \approx 0.56$. Above this velocity, solitons pass through the defect without significant interaction, merely losing some velocity and a little mass to the defect

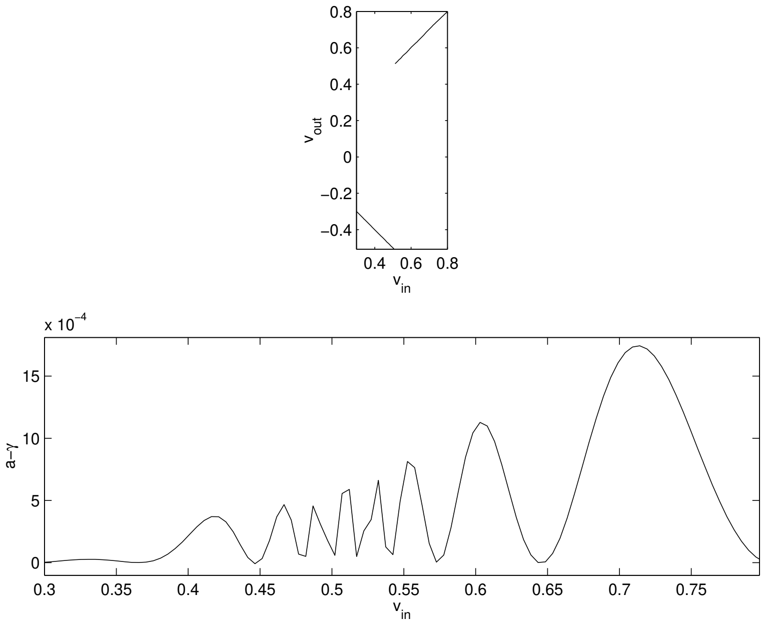

Figure 4.1: (Top) Outgoing velocity vs. incoming velocity of solitons incident on the defect via ODE simulation with $\eta = \frac{1}{2}$. (Bottom) Amplitude $a - 1$ of nonlinear defect mode after passing of the soliton; note vertical scale is $\mathcal{O}(10^{-3})$.

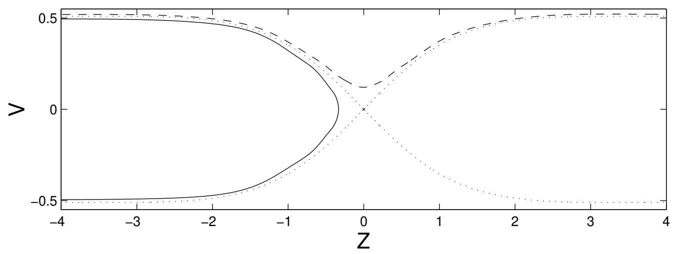

Figure 4.2: Phase space projections of trajectories above (solid) and below v_c (dashed), showing strong evidence for a saddle point. Projections of stable and unstable manifolds of the saddle on $\mathcal{P}_0$ are shown as dotted curves.

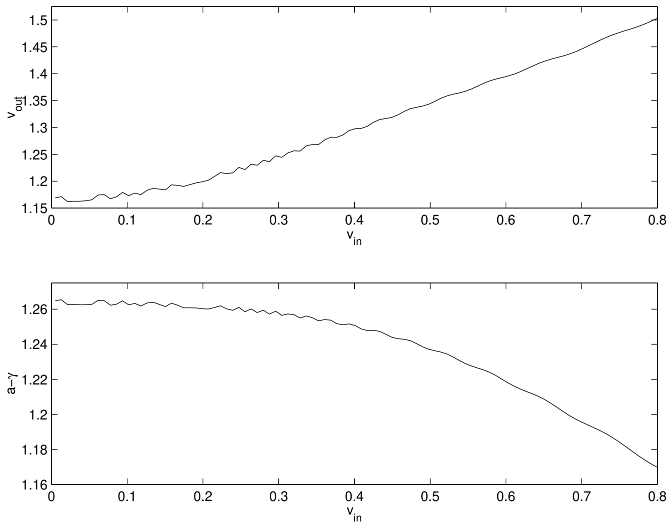

Figure 4.3: (Top) Outgoing velocity vs. incoming velocity of solitons incident on defect via ODE simulation with $\eta = 2$. (Bottom) Amplitude $a - 1$ of nonlinear defect mode after passing of the soliton.

mode. Below v_c, however, the soliton interacts with the defect a finite and apparently random number of times before being ejected either to the right or the left. It is also striking that the amount of energy left in the defect mode seems to be restricted to two levels: either $a - 1 \approx 3$ or $a - 1 \ll 1$. The behavior is apparently governed by the behavior at $|Z| = \infty$. Since there exist solutions to (3.12) with Z bounded, as well as solutions which approach $Z = \infty$ with $V > 0$, these must be separated by solutions for which $Z \to \infty$ while $V \to 0$.

Figure 4.5 shows the (Z, V) projections of trajectories with nearby initial velocities on either side of v_c ($V(0) = v_c \pm .002$). The solid curve comes close to the stable manifold of infinity $W^s(\mathcal{P}_\infty)$ from below and is transiently captured before eventual reflection, while the dashed curve approaches infinity with V bounded above zero, and is transmitted without further interaction. This sensitive dependence is reminiscent of that found in our earlier study of an ODE model of kink-defect interaction in the sine-Gordon equation [3], and shown there to be related to the homoclinic tangle formed by transverse intersection of stable and unstable manifolds of periodic orbits at $|Z| = \infty$, which would correspond to $W^{s,u}(\mathcal{P}_\infty)$ in the present case. Compare Figure 4.4 with Figure 3.2 of [3].

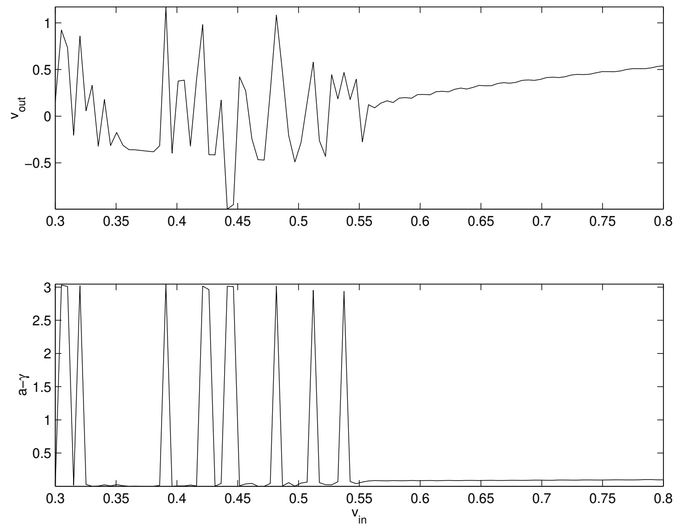

Figure 4.4: (Top) Outgoing velocity vs. incoming velocity of solitons incident on defect via ODE simulation with $\eta = 4$. (Bottom) Amplitude $a - 1$ of nonlinear defect mode after passing of the soliton. **XYZ - update with better quality calcs!**

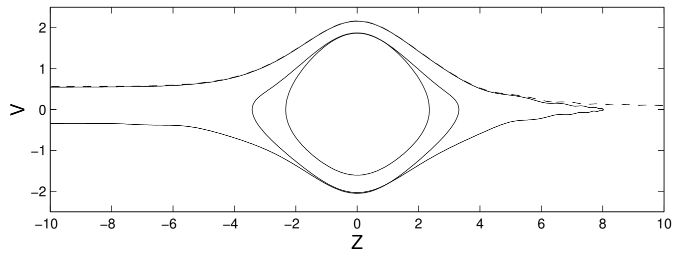

Figure 4.5: (Z, V) phase space plots of captured and transmitted trajectories just above and below critical velocity.

5 The structure of invariant manifolds

For small values of η, the soliton traveling near the critical velocity appears to approach a hyperbolic fixed point or periodic orbit on $\mathcal{P}_0$: see Figure 4.2. For larger values of η, the soliton oscillates about $\mathcal{P}_0$ as it would around an elliptic fixed point: see Figure 4.5. To obtain a (partial) understanding of the global phase space structure of (3.12) and how the incoming soliton orbits lie within it, we now return to a more detailed analysis of these ODEs.

5.1 Stability of orbits on $\mathcal{P}_0$

We first analyse the stability types of relevant orbits in $\mathcal{P}_0$, on which ODEs reduce to:

$$\dot{\psi} = \frac{c^2}{2} - ca + (c-a) + \frac{(2a^2 - ac - 1)}{\sqrt{a^2-1}} \cos\psi, \tag{5.1a}$$

$$\dot{a} = -(c-a)\sqrt{a^2-1}\sin\psi. \tag{5.1b}$$

Typical phase portraits of (5.1) are shown in Figure 3.1 above.

Consider the solution $\mathcal{S}^*$ to the initial value problem of a soliton starting from $|Z| = \infty$ with finite velocity V_∞ and zero energy in the defect mode, i.e. $a = 1$ and $c = \eta + 1$[1]. $\mathcal{S}^*$ is confined to the level

$$H = -\frac{c^3}{3} + (c-1)(c + V_\infty^2) \stackrel{\text{def}}{=} H_\infty \tag{5.2}$$

of the conserved Hamiltonian and hence, if it approaches $\mathcal{P}_0$, can only interact with orbits having the same H-value. In particular, since the maximum H value for orbits on $\mathcal{P}_0$ is assumed by the fixed point (π, a^*), there is a critical velocity $V_\infty^{\max}$ above which the solutions $\mathcal{S}^*$ have more 'energy' than any orbits contained in $\mathcal{P}_0$, and thus must remain bounded away from it. Similarly, the minimal value $H = -c^3/3 + c(c-1)$ of orbits $\mathcal{S}^*$, assumed when $V_\infty = 0$, bounds the set of accessible orbits on $\mathcal{P}_0$, as already shown on Figure 3.1.

Consequently, for each $V_\infty \in [0, V_\infty^{\max})$, we find a periodic orbit $\mathcal{S}_0 \in \mathcal{P}_0$ with the same Hamiltonian value $H = h_0$ as $\mathcal{S}^*$ and determine its stability by examining the linearization of the full system (3.12) about $\mathcal{S}_0 = (0, 0, \psi_{\mathcal{P}}(t), a_{\mathcal{P}}(t))$. The stability of such an orbit is given by the eigenvalues of the monodromy matrix: the fundamental solution matrix of the linearized differential equation evaluated at one period of oscillation. Let $\tilde{\mathcal{S}}_0 = (\tilde{Z}, \tilde{V}, \tilde{\psi}, \tilde{a})$ solve this linearized ODE, which is block-diagonal, with the $(\tilde{Z}, \tilde{V})$ components decoupling from the $(\tilde{\psi}, \tilde{a})$ components. The eigenspace of the latter coincides with $\mathcal{P}_0$ and hence they have eigenvalues of unit modulus, as one expects from the integrable structure of Figure 3.1 (in fact $\lambda = 1$ with multiplicity two and a single eigenvector).

[1]Practically, as in Section 4, the orbit is started at some $|Z_0| \gg 1$ with $a = 1 + \varepsilon$, $\varepsilon \ll 1$.

Perturbations perpendicular to $\mathcal{P}_0$ satisfy

$$\begin{aligned}
\frac{d}{dt}\tilde{Z} &= (c - a_{\mathcal{P}}(t))\tilde{V}, \\
\frac{d}{dt}\tilde{V} &= -\left((c - a_{\mathcal{P}}(t))^2 + (c - a_{\mathcal{P}}(t))\sqrt{a_{\mathcal{P}}(t)^2 - 1}\cos\psi_{\mathcal{P}}(t)\right)\tilde{Z}.
\end{aligned} \tag{5.3}$$

Since this may be written in the form

$$\frac{d}{dt}\begin{pmatrix}\tilde{Z}\\ \tilde{V}\end{pmatrix} = \begin{pmatrix}0 & A_{1,2}(t)\\ A_{2,1}(t) & 0\end{pmatrix}\begin{pmatrix}\tilde{Z}\\ \tilde{V}\end{pmatrix},$$

the Floquet theory for Hill's equation is applicable [6]. The product of the Floquet eigenvalues must be one, and their sum is given by the Floquet discriminant. If this is greater than two in absolute value, the periodic orbit is hyperbolic, i.e. unstable; if less than two, the orbit is elliptic, i.e. neutrally stable, transverse to $\mathcal{P}_0$. We compute these discriminants numerically by first computing the orbit $(a_{\mathcal{P}}(t), \psi_{\mathcal{P}}(t))$ for one period using the Runge-Kutta method. We then compute the fundamental solution matrix for the linearized system (5.3) numerically, using interpolated data for the coefficients.

Since each periodic orbit in $\mathcal{P}_0$ corresponds, via its Hamiltonian level, to a velocity V_∞ at $|Z| = \infty$, we plot in Figure 5.1 the Floquet discriminants as functions of V_∞ for the three examples of Section 4.1. In the first case, with $\eta = \frac{1}{2}$, all orbits are hyperbolic. It is notable that $V_\infty^{\max} = 0.51$ in this case, approximately equal to the critical velocity for transmission and reflection seen in Figure 4.1 (but see the detailed analysis in section 5.2, below). In contrast, the velocity range shown in Figure 4.4 is seen here to correspond to periodic orbits of *elliptic* type, consistent with the intuition from Figure 4.5, that solutions oscillate about $\mathcal{P}_0$. The critical velocity for capture and transmission of Figure 4.4 is indicated by an asterisk in the third panel of 5.1.

Some interesting implications can immediately be drawn from the stability types of orbits in $\mathcal{P}_0$ implicit in Figure 5.1. Recall that these periodic orbits correspond to a state in which a soliton, stalled over the defect at $Z = 0$, exchanges energy periodically with the defect mode. Hence, if soliton and defect parameters are chosen consistent with a stable region (eg., below $V_\infty \approx 0.9$ in case two and for $V_\infty < 1$ and $V_\infty \in (1.4, 1.8)$ in case three), and the soliton is initialized at the defect or somehow introduced into it, perhaps by temporarily destabilizing the relevant orbit, it will remain trapped under small perturbations.

In the case $\eta = 0.5$, the initial condition $\mathcal{S}_c^* = (-\infty, V_c = 0.501, 1, \psi_0)$ is on the same Hamiltonian surface as this fixed point. The stable and unstable manifolds of (π, a^*) are only one-dimensional and thus cannot separate reflected from transmitted orbits. However, the stable and unstable manifolds of (the accessible disk on) $\mathcal{P}_0$ are three dimensional, and are consequently able to divide the phase space into disjoint regions. We must therefore compute the stable and unstable manifolds of the accessible periodic orbits on $\mathcal{P}_0$ as well as of the saddle-center (π, a^*).

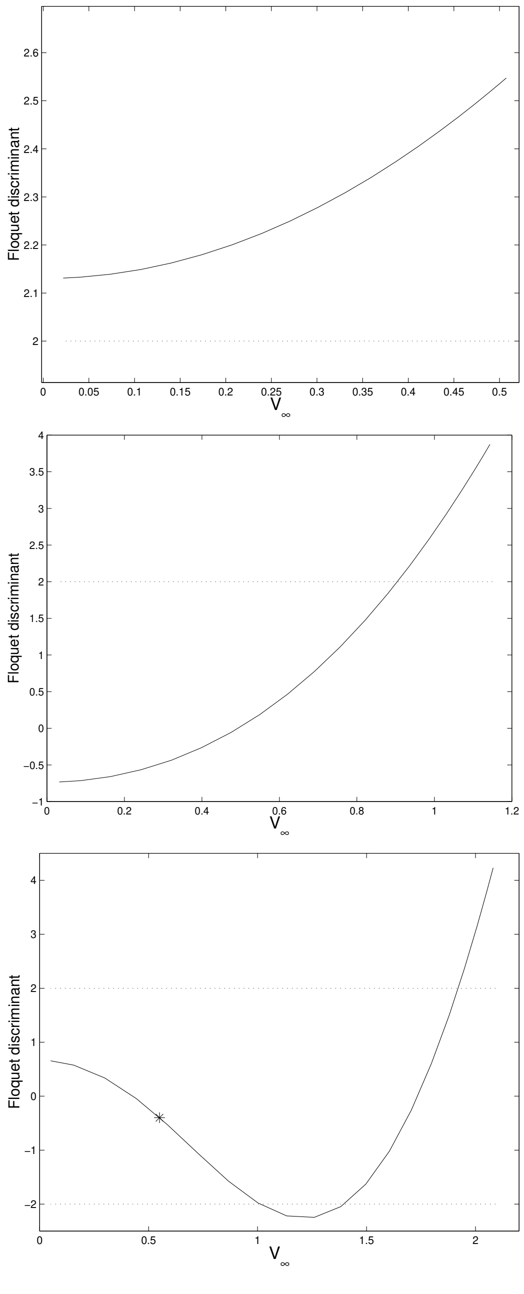

Figure 5.1: The Floquet discriminant vs. incoming velocity for $\eta = \frac{1}{2}, 2, 4$ respectively (top to bottom). In the third figure, the critical velocity separating capture from transmission is marked with an asterisk.

5.2 Stable and unstable manifolds of $\mathcal{P}_0$

Appealing to the symmetries of (3.13) and the fact that the orbits of interest are reflection-symmetric about $\psi = \pi$, we need only compute one of the four branches of $W^{s,u}(\mathcal{S}_0)$ for each of the saddle type periodic orbits $\mathcal{S}_0 \in \mathcal{P}_0$. To do this we first compute each periodic orbit $\mathcal{S}_0$ starting at a point $(a, \psi) = (a_0, \pi)$ where $a_0 > a^*$, the saddle-center. We interpolate these with 64 equally-spaced points (with respect to time). At each of these 64 points (a_0, ψ_0), the fundamental solution matrix is computed as in Subsection 5.1. Fourier interpolation is used to compute the coefficients $(a_\mathcal{P}, \psi_\mathcal{P})$ at intermediate times, so the orbit $\mathcal{S}_0$ need only be computed once. At each point on the periodic orbit, we compute the unstable eigenvector of the monodromy matrix, $\vec{v}_0 = (Z_0, /V_0)^T$. We normalize it so that $|\vec{v}_0| = 10^{-5}$ and solve the full system (3.12) of ODE's with initial conditions (Z_0, V_0, a_0, ψ_0), stopping when $|Z| = 20$.

Let $W^s(\mathcal{P}_0) = \cup_{h_0} W^s(\mathcal{S}_0)$ denote the set of stable manifolds of the accessible hyperbolic orbits in $\mathcal{P}_0$. $W^s(\mathcal{P}_0)$ is three dimensional, and is locally (near $|Z| = 0$) foliated by two dimensional cylinders, each of which is a local stable manifold of some $\mathcal{S}_0$. We therefore expect $W^s(\mathcal{P}_0)$ to intersect the three-dimensional cross sections of initial data $\Sigma_\pm = \{(V, \psi, a) | Z = \pm Z_0, |Z_0| \gg 1\}$ in two-dimensional sets, which should in turn separate sets of initial data giving rise to solutions that pass the defect from those reflected by it.

Figure 5.2 shows the results of computations for the first of the three cases of Section 4: $\eta = 1/2$, and for a second case, with slightly larger $\eta = 0.75$. Note that the sets $\Sigma_\pm \sim \mathbb{R} \times S^1 \times \mathcal{I}$ are periodic in ψ. As might be expected from the experiment of Section 4.1, near $a = 1$ the surface $W^s(\mathcal{S}_0) \cap \Sigma_-$ is a graph over the (ψ, a) annulus: all orbits starting at points below it are reflected, and points starting above it are transmitted. Further from $a = 1$ the surface develops folds; these become more pronounced for higher η (c): see lower panel of Figure 5.2. The surface describes critical velocity as a function of phase ψ and amplitude $a - 1$ of the defect mode. Note the weak phase dependence, particularly as $a \to 1$, and that the surface approaches $a = 1$ at $V \approx 0.54$ in the case $\eta = 0.5$ (upper panel); this is the critical velocity found in Section 4.1. Initial data on this surface corrsponds to trapping (recall that the accessible orbits in $\mathcal{P}_0$ correspond to solitons pinned at the defect).

XYZ : Needs updating - number 0.51 was cited before.

In interpreting this figure it is helpful to note the following facts. Individual two-dimensional components $W^s(\mathcal{S}_0)$ of $W^s(\mathcal{P}_0)$ intersect sections at $Z = \pm Z_0$ for small $|Z_0|$ in homotopically trivial (contractible) circles, but as $|Z|$ (and the time of flight) increases, particular solutions belonging to $W^s(\mathcal{S}_0)$ can pass arbitrarily close to the degenerate saddles on $a = 1$ at $\psi = \pi/2, 3\pi/2$. This effectively separates neighboring solutions and stretches their phase (ψ) angles over a range exceeding 2π. The result is that the corresponding sets $W^s(\mathcal{S}_0) \cap \Sigma_-$ extend around the S^1 component in a homotopically nontrivial manner. Only those components of $W^s(\mathcal{P}_0)$ very close to $W^s(\pi, a^*)$ remain contractible; these can be seen in Figure 5.2 near $\psi = \pi, a = 1$.

The 'outer' (lower V, higher a) boundary of the computed portion of $W^s(\mathcal{S}_0) \cap$

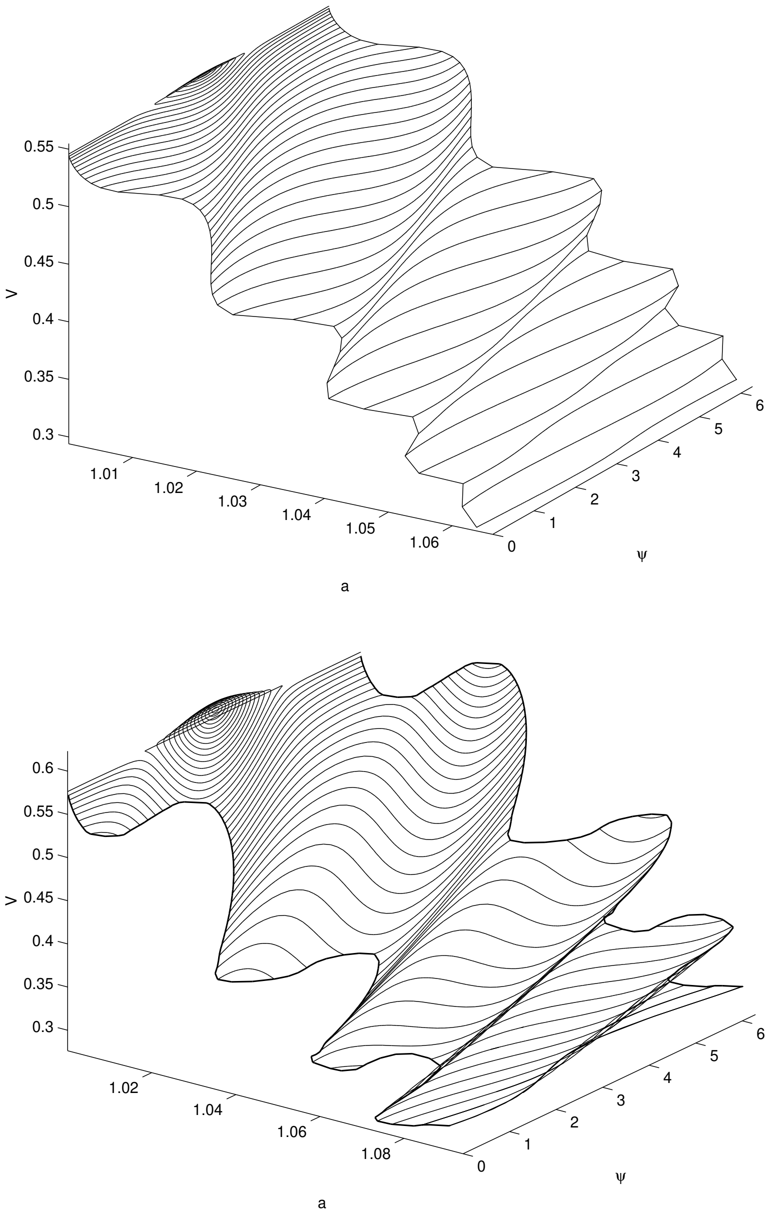

Figure 5.2: Part of the intersection of the stable manifold of $\mathcal{P}_0$ with Σ_-. Upper panel, $\eta = 0.5$ ($c = 1.5$); lower panel, $\eta = 0.75$ ($c = 1.75$).

Σ_- is limited by numerical issues: it is impossible to compute with uniform accuracy as velocities approach zero, since the time of flight grows without bound; however, it appears that velocities do decrease to zero as a increases. For example, numerical experiments like those of Section 4.1 indicate that all orbits launched with positive velocities, no matter how small, and $a > 1.1$, are transmitted. The surface therefore intersects $V = 0$.

We will include computations of invariant manifolds for the medium and large η cases in an extended version of this paper. Preliminary studies suggest that, as c increases, the set $W^s(\mathcal{P}_0) \cap \Sigma_-$ 'separates' from the plane $a = 1$, so that nearby initial data all lie in the transmission zone. However, as c continues to increase, the stable manifold $W^s(\mathcal{P}_\infty)$ evidently invades Σ_-, leading to the complex behavior of Figures 4.4-4.5. The increased folding of $W^s(\mathcal{S}_0) \cap \Sigma_-$ as η (or c) increases evident in Figure 5.2 is consistent with the existence of a fine (fractal) structure suggested by Figure 4.4. We conjecture that, as $W^s(\mathcal{P}_\infty)$ invades Σ_-, since it cannot intersect $W^s(\mathcal{S}_0)$, it must 'align' with the latter (folded) manifold, producing (infinitely) many regions of transmission and reflection on any vertical line in Σ_- above the (a, ψ)-plane.

6 Interpretation and Summary

In this paper – a work in progress – we have derived a finite dimensional model for soliton-defect mode interactions in a nonlinear Schrödinger equation with a point defect. Following [2], and allowing for a fully nonlinear defect mode, which by itself is an exact solution, we derive a three-degree-of-freedom Hamiltonian system that describes the evolution of amplitudes and phases of the soliton and defect mode, and the position and velocity of the former. Allowing a nonlinear defect mode is important, since it permits resonant energy transfer to occur over a range of soliton amplitudes. However, only these two modes are represented; in particular, radiation to the continuum is ignored.

The resulting ODEs may be further reduced to two degrees of freedom, since in addition to the Hamiltonian, a second quantity, corresponding to the total energy in the two modes, is also conserved. While this system is rather complex, and appears to be nonintegrable, it possesses two-dimensional invariant subspaces filled with periodic orbits, whose stable and unstable manifolds partially determine the global structure of solutions. We use this system to investigate the reflection, transmission, and trapping of solitons launched 'from infinity,' by the defect, concentrating on the case in which the energy intially all resides in the soliton. Numerical simulations reveal three basic types of behavior:

1. For small initial soliton energies, reflection or transmission occurs for almost all initial velocities. Specifically, a unique trapping velocity exists for each initial phase and defect amplitude below a critical level; this corresponds to initial data on the stable manifold of a subset of periodic orbits, each of which corresponds to the soliton stalled over the defect and periodically exchanging energy with the defect mode.

2. For moderate initial soliton energies, all solitons are transmitted unless there is sufficient initial energy in the defect mode, in which case a scenario similar to the large soliton energy case ensues.

3. For large initial soliton energies, there is a critical velocity above which all solitons are transmitted; below this, a complex structure of reflection and transmission bands exists, separated by trapping regions that apparently are of measure zero.

We expect that a more complete understanding of the second and third cases will follow from our ongoing computations of invariant manifolds. We also intend to compare the ODE studies with direct numerical integrations of the original PDE.

Acknowledgements: RG was supported by NSF DMS-9901897 and Bell Laboratories/Lucent Technologies under the Postdoctoral Fellowship with Industry Program. PH was partially supported by DoE: DE-FG02-95ER25238. We thank D. Pelinovsky for stimulating discussions early in this project.

Appendix: Computational details

We verify the claim that the fixed points $(\psi, a) = (\pi, a^*)$ on $\mathcal{P}_o$ are saddle centers. The center behavior within $\mathcal{P}_0$ follows from the structure of the restricted Hamiltonian (3.14), and behavior transverse to $\mathcal{P}_0$ is determined by the linearization given in (5.3), evaluated at (π, a^*). The resulting (constant) matrix has zero trace and determinant

$$D = (c - a^*)^2 \left((c - a^*) - \sqrt{(a^*)^2 - 1} \right) \stackrel{\text{def}}{=} (c - a^*)^2 \tilde{D}(a^*), \tag{6.1}$$

so, provided $\tilde{D}(a^*) < 0$, the remaining eigenvalues $\lambda = \pm\sqrt{-D}$ are real, implying hyperbolic saddle type behavior in the (Z, V) directions. Note that $\tilde{D}(a^*) < 0$ iff

$$a^* > a_c = \frac{c^2 + 1}{2c}. \tag{6.2}$$

From (5.1) the fixed point value a^* is given by solution of

$$L(a) \stackrel{\text{def}}{=} \frac{c^2}{2} + c - (c + 1)a = \frac{(2a^2 - ca - 1)}{\sqrt{a^2 - 1}} \stackrel{\text{def}}{=} R(a). \tag{6.3}$$

Now $L(a)$ is monotonically decreasing and $R(a)$ is monotonically increasing (in the range $a \in (1, c)$), so if we can show that $L(a_c) > R(a_c)$, it follows that $a^* > a_c$ and hence that $\tilde{D}(a^*) < 0$, as required. But

$$L(a_c) = \frac{(c^2 - c - 1)}{2c} \text{ and } R(a_c) = \frac{1}{c},$$

and so the claim is true.

References

[1] J.C. Bronski, *Nonlinear scattering and analyticity properties of solitons*, Nonlinearity **8 (2)** (1998), 161–182.

[2] K. Forinash, M. Peyrard, and B. Malomed, *Interaction of discrete breathers with impurity modes*, Phys. Rev. E **49** (1994), 3400–3411.

[3] R. H. Goodman, P. J. Holmes, and M. I. Weinstein, *Interaction of sine-Gordon kinks with defects: Phase space transport in a two-mode model*, Physica D (to appear) (2002).

[4] R. H. Goodman, R. E. Slusher, and M. I. Weinstein, *Stopping light on a defect*, submitted to J. Opt. Soc. Am. B (2001).

[5] J. Guckenheimer and P. Holmes, *Nonlinear Oscillations, Dynamical Systems, and Bifurcations of Vector Fields*, Springer-Verlag, New York, 1983.

[6] P. Hartman, *Ordinary Differential Equations*, second, corrected ed., Wiley Publishing Co., New York., 1964.

[7] P. Holmes and J.N. Kutz, *Dynamics and bifurcations of a planar map modelling dispersion-managed breathers*, SIAM J. on Appl. Math. **59** (1999), 1288–1302.

[8] Y.S. Kivshar, S.A. Gredeskul, A. Sánchez, and L. Vázquez, *Localization decay induced by strong nonlinearity in disordered systems*, Phys. Rev. Lett. **64 (15)** (1990), 1693–1696.

[9] J.N. Kutz, P. Holmes, S.G. Evangelides, and J.P. Gordon, *Hamiltonian dynamics of dispersion managed breathers*, J. Opt. Soc. America B **15 (1)** (1998), 87–96.

[10] R. McGehee, *A stable manifold theorem for degenerate fixed points with applications to celestial mechanics*, J. Differential Equations **14** (1973), 70–88.

[11] V. K. Melnikov, *On the stability of the center for time periodic perturbations*, Trans. Moscow Math. Soc. **12** (1963), 1.

[12] V. Rom-Kedar and S. Wiggins, *Transport in two-dimensional maps*, Arch. Rational Mech. and Analysis **109** (1990), 239–298.

[13] S. Wiggins, *Chaotic Transport in Dynamical Systems*, Springer-Verlag, New York, 1992.